

# Radiometric Calibration Stability of the FIRST: a Longwave Infrared Hyperspectral Imaging Sensor

Vincent Farley<sup>\*a</sup>, Martin Chamberland<sup>a</sup>, Alexandre Vallières<sup>a</sup>,  
André Villemaire<sup>a</sup>, and Jean-François Legault<sup>b</sup>

<sup>a</sup>Telops inc., 100-2600 St-Jean-Baptiste, Québec, Qc, Canada G2E 6J5

<sup>b</sup>Telops USA inc., 3201 Stellhorn Road, Fort Wayne, Indiana 46815, USA

## ABSTRACT

Emerging applications in Defense and Security require sensors with state-of-the-art sensitivity and capabilities. Among these sensors, the imaging spectrometer is an instrument yielding a large amount of rich information about the measured scene. Standoff detection, identification and quantification of chemicals in the gaseous state are fundamental needs in several fields of applications. Imaging spectrometers have unmatched capabilities to meet the requirements of these applications.

Telops has developed the FIRST, a LWIR hyperspectral imager. The FIRST is based on FTIR technology to yield high spectral resolution and to enable high accuracy radiometric calibration. The FIRST, a man portable sensor, provides datacubes of up to 320×256 pixels at 0.35 mrad spatial resolution over the 8-12 μm spectral range at spectral resolutions of up to 0.25 cm<sup>-1</sup>. The FIRST has been used in several field measurements, including demonstration of standoff chemical agent detection. One key feature of the FIRST is its ability to give calibrated measurements. The quality of the radiometric and spectral calibration will be presented in this paper.

During the field measurements, the FIRST operated under changing environmental conditions while many calibration measurements were taken. In this paper, we will present the stability of the calibration of the FIRST obtained during the field campaigns.

Keywords: hyperspectral imaging, imaging FTS, FTIR, standoff detection, remote sensing, radiometric calibration, thermal infrared

## 1. Introduction

The absolute radiance accuracy of a remote sensing instrument is one of its fundamental characteristics. Physical parameters derived from field spectra are directly affected by the ability of the sensor to produce measurements with good radiometric fidelity. The radiometric calibration of FTIR instruments used for remote sensing was developed and refined in the late 1980s [1]. The result of this work yielded a simple and powerful calibration approach that corrects for instrument response, accurately removes the instrument self-emission and corrects for phase characteristics of the FTIR.

The stability of the radiance accuracy over time, often referred to as the radiometric stability, is equally important. It dictates the frequency at which the radiometric calibration process needs to be performed. In this paper, a large quantity of experimental calibration data acquired during two field campaigns in the summer of 2005 is used to analyze the radiometric stability of the Telops FIRST sensor (Field-portable Imaging Radiometric Spectrometer Technology). This study has the flavor of similar studies that were performed on other FTIR sensors, e.g. the study of the DRDC Valcartier CATSI radiometric stability presented in [2].

The FIRST spectral calibration is also addressed in this paper. The spectral calibration of a sensor is another important aspect, especially for applications that require a narrow spectral resolution and a good spectral accuracy. The spectral calibration can be performed by identifying thin spectral references in the acquired spectra, such as gas absorption or emission lines. Since it is present in the atmosphere, the most practical gas used in the LWIR band is water vapor.

---

\* vincent.farley@telops.com; phone (418) 864-7808; fax (418) 864-7843; www.telops.com

The FIRST sensor is described in Section 2. Section 3 presents the radiometric calibration concept. The experimental data used for the analysis is introduced in Section 4. Section 5 consists in the radiometric stability analysis. Finally, the sensor spectral calibration is presented in Section 6.

## 2. Description of the FIRST-LW Sensor

The FIRST sensor is a lightweight and compact spectroradiometer. The spectral measurements are performed using a Fourier-Transform Spectrometer (FTS). It uses a 320x256 LWIR PV-MCT focal plane array detector that can be windowed and formatted to fit the desired size and to decrease the acquisition time. Spectral resolution is user-selectable from 0.25 to 150  $\text{cm}^{-1}$ . This instrument measures the complete spectrum of each pixel in the image, each pixel having an instantaneous field-of-view of 0.35 mrad. The latest version of this field-portable sensor is shown in Figure 1. This version is conduction-cooled and sealed from the environment. It is thus ideally designed to withstand operation in harsh and dusty conditions.

The instrument features 2 internal calibration blackbodies used to perform a complete end-to-end radiometric calibration of the measurements (see Section 3). In its longwave IR version, the instrument has good sensitivity over the 8-12  $\mu\text{m}$  band. This spectral band is ideal for standoff chemical agent detection at ambient temperatures. The sensor also has acquisition and processing electronics, including 4 GB of high-speed DDR-SRAM, with the capability to convert the raw interferograms into spectra using real-time Discrete-Fourier Transform (DFT).



Figure 1: Photograph of the FIRST sensor

The instrument outputs the measurements on a high-speed CameraLink interface. The configuration, monitoring and real-time housekeeping data collection is performed using an Ethernet link. A bore-sight video camera takes simultaneous visible images aligned with the imaging FTS. The instrument supports two operating modes: FTS mode and Camera mode. In Camera mode, the instrument generates a standard broadband thermal IR digital video and supports up to 300 frames per second with the full 320x256 pixels of the focal plane array area. In FTS mode, the interferograms or the spectra are transferred along with a header containing all configuration parameters and monitored values to be stored on the computer.

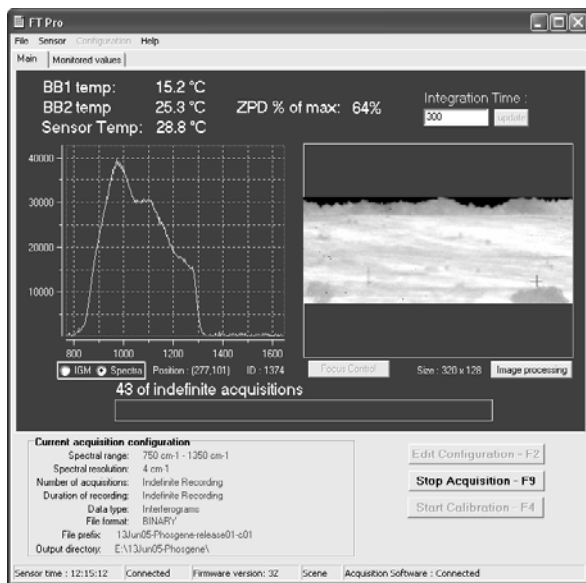


Figure 2: FTPro™ control software

The FTPro™ control software provides a user-friendly interface, giving real-time feedback to the operator. A screenshot of the control software is presented in Figure 2 on the left-hand side. On the right panel, the non-uniformity corrected broadband IR image is displayed in grayscale where black corresponds to low radiance level and white corresponds to high radiance level. The uncalibrated raw spectrum (or the interferogram as selected by the operator) of a selected pixel in the image is displayed in real time on the left of the screen. Additional key parameters such as the blackbodies temperature, the sensor temperature and the level of signal on the FPA are also displayed. Additional monitored values can be viewed in a separate panel. This main panel of the user interface is used to start the acquisition of the data or to initiate calibration measurements. The configuration of the sensor (image size and location, spectral resolution, blackbody and sensor temperatures, etc...) is performed with another input panel. The integration time of the FPA can be changed from the main panel.

The sensor has the capability to change the focus of the IR image to produce a clear image at any distance from 2 meters up to infinity. The FIRST was presented in detail in previous papers [3, 4, 5 and 6].

### 3. Radiometric Calibration Concept

The basic approach for determining the absolute radiance measured by a Fourier transform spectrometer (FTS) has been well described in the late 1980s [1]. This process called radiometric calibration basically consists in characterizing the FTS response by a linear expression, i.e. by a gain (or slope) and an offset. The gain and offset are characterized as a function of the wavelength, and they are complex to characterize the phase of the FTS as well. This gain and offset include the response of the interferometer, of the detector and of the associated electronics. Thus, the linearity of the detector and associated electronics is important.

The FTS measurement can be expressed as follows:

$$\overline{M}(\sigma) = \overline{G}(\sigma) \cdot (L(\sigma) + \overline{O}(\sigma)) \quad (1)$$

where  $\overline{M}(\sigma)$  is the complex spectrum from the instrument measurement; [a.u.(arbitrary units)]  
 $\overline{G}(\sigma)$  is the complex instrument gain; [a.u. / (W/m<sup>2</sup>·sr·cm<sup>-1</sup>)]  
 $L(\sigma)$  is the scene true spectral radiance; [W/m<sup>2</sup>·sr·cm<sup>-1</sup>] and  
 $\overline{O}(\sigma)$  is the complex instrument offset. [W/m<sup>2</sup>·sr·cm<sup>-1</sup>]

*Overbars refer to complex quantities, comprising a real and an imaginary part.*

The instrument gain and offset can be determined by measuring the radiance of two known reference targets. Blackbodies at known temperatures are generally used as reference targets. Their theoretical radiance follows the Planck relation:

$$L_{BB}(\sigma, T) = \frac{2hc^2\sigma^3}{e^{hc\sigma/k_B T} - 1} \quad (2)$$

where  $L_{BB}(\sigma, T)$  is the blackbody spectral radiance; [W/m<sup>2</sup>·sr·cm<sup>-1</sup>]  
 $h$  is the Planck constant; [6.63×10<sup>-30</sup> cm<sup>2</sup>·kg/s]  
 $c$  is the speed of light; [3.00×10<sup>10</sup> cm/s]  
 $\sigma$  is the wavenumber; [cm<sup>-1</sup>]  
 $k_B$  is the Boltzmann constant; [1.38×10<sup>-19</sup> cm<sup>2</sup>·kg/s<sup>2</sup>·K] and  
 $T$  is the blackbody temperature; [K]

The acquisition of the blackbody measurements at two temperatures is required in order to write Equation (1) for both the cold and hot blackbody temperatures. This two equations system is then solved to yield:

$$\overline{G}(\sigma) = \frac{M_H(\sigma) - M_C(\sigma)}{L(\sigma, T_H) - L(\sigma, T_C)} \quad (3)$$

$$\overline{O}(\sigma) = \frac{M_C(\sigma) \cdot L(\sigma, T_H) - M_H(\sigma) \cdot L(\sigma, T_C)}{M_H(\sigma) - M_C(\sigma)} \quad (4)$$

where the  $H$  and  $C$  subscripts refer to the hot and cold blackbody respectively.

A few assumptions are made in this analysis. First, it is assumed that the detector has a linear response. Second, it is assumed that the blackbodies have a unity emissivity and a perfectly known and uniform surface temperature.

#### 4. Experimental Data

The FIRST sensor was used in two major field campaigns in the summer of 2005. First, it was used in a four-week campaign in England in June 2005. This trial was held at Dstl in Salisbury. Telops staff operated the FIRST sensor during this campaign aimed at testing standoff gas detection with remote sensors. The gas detection results are presented in [6]. A photograph of the sensor at the Salisbury trial is shown in Figure 3.

Second, the FIRST sensor was used in a two-week field campaign in Utah in July 2005. This trial was held at Dugway Proving Grounds near Salt Lake City. Staff from the Johns Hopkins University Applied Physics Laboratory operated the loaned Telops FIRST sensor in this campaign. They shared their data with Telops for the purpose of this study.



**Figure 3: FIRST sensor at the Dstl campaign in Salisbury**

The calibration data acquired during these two field campaigns was analyzed in order to study the FIRST radiometric stability. 120 radiometric calibrations were performed during the Salisbury trial, and 41 radiometric calibrations were performed during the Dugway campaign. Thus, the experimental data consists in a total of 161 radiometric calibrations acquired in two different continents over a 2-month time interval.

All the results presented in this paper are based on this data. Figure 4 shows the ambient temperature and the sensor temperature (measured on the modulator) over the entire time of the field campaigns. The ambient temperature varied between 15 and 33°C, and the sensor temperature varied between 18 and 42°C. Note that the zero time reference is 7 June 2005 at midnight.

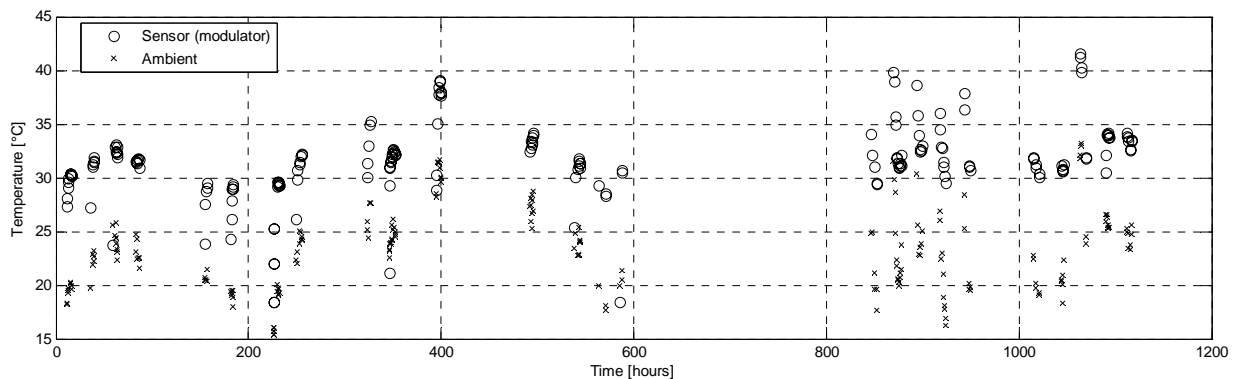


**Figure 4: Ambient and sensor temperatures during the field campaigns. Seemingly vertical groups represent the usual daily temperature increase or nocturnal decrease.**

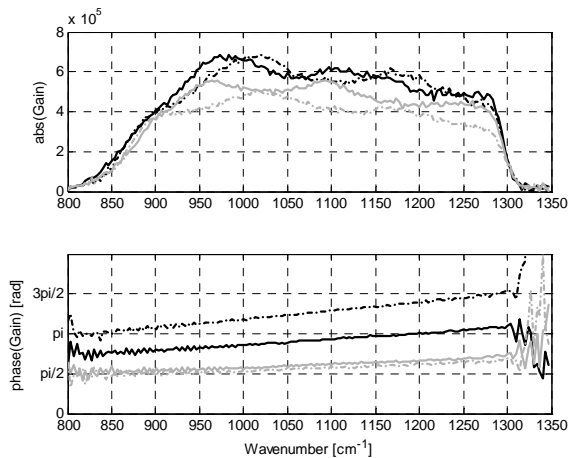
The sensor was operated with fixed parameters during the two campaigns. The parameters are a centered spatial window of  $320 \times 128$  pixels, a spectral resolution of  $4 \text{ cm}^{-1}$ , a focus adjustment at infinity and blackbody temperatures adjusted to approximately 5 degrees below and above ambient temperature (for the cold and hot reference targets).

Note that during the two field campaigns, the FIRST sensor was used without taking advantage of its sensor temperature stabilization feature. This feature consists in heaters that are strategically positioned on the sensor key parts; i.e. the interferometer and the lens mechanical assemblies. These heaters can be used to maintain the instrument temperature stable regardless of the ambient temperature fluctuations. By disabling this feature, the data acquired allowed to evaluate the radiometric stability as a function of the instrument temperature fluctuations.

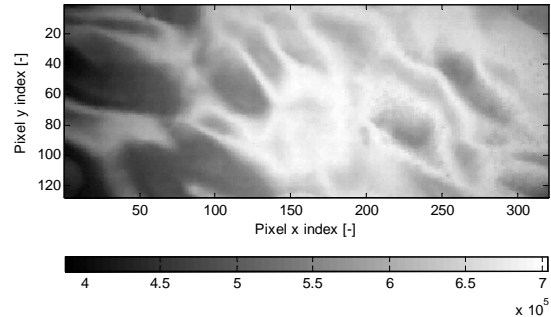
## 5. Experimental Radiometric Calibration Stability Analysis

Figure 5 shows the magnitude and phase of one measurement of the sensor radiometric gain. The result is shown for 4 pixels selected randomly out of the 40,960 pixels of the 320×128 window that was used in the field campaigns. The gain magnitude decrease in the 850 cm<sup>-1</sup> region is caused by the detector cut-off, while the gain decrease around 1300 cm<sup>-1</sup> is due to the presence of an optical cold filter in front of the detector. One can see that the gain magnitude of each pixel has a spectral signature that varies relative to the other pixels. This is believed to be caused by channeling in the detector surface layer (Fabry-Perot effect). Figure 6 shows the spatial gain magnitude at 10μm, and Figure 7 shows the spatial broadband gain magnitude. It is clear that there is a significant advantage to characterize the gain as a function of the wavelength, as a lot of spectral variations are not considered if only a broadband calibration is performed. This illustrates an advantage that a spectral sensor has over a broadband sensor to achieve accurate radiometry.

The phase of the gain is very linear, as shown in Figure 5. This is an indication of a well compensated instrument. Also, the phase of the gain is different for different pixels. Figure 8 shows the spatial phase of the gain. The sinusoidal phase fluctuation is due to a slight wavefront shear in the modulator. This affects the phase with a sinusoidal shape in the axis of the shear (almost perfectly horizontal in this case). Having a phase shift of 0.55 period at 1000 cm<sup>-1</sup> (8.7 periods at the metrology wavelength) over the entire FPA indicates that the phase shift for a single pixel is < 0.2% of a period at 1000 cm<sup>-1</sup>. This level of wavefront shear has a completely negligible effect on the modulation efficiency.



**Figure 5: Gain of 4 random pixels**



**Figure 6: Spatial map of gain magnitude at 10μm**

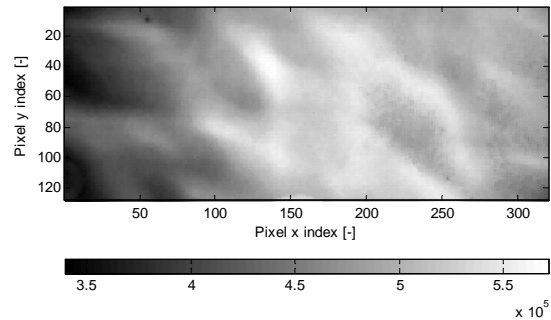


**Figure 7: Spatial map of broadband gain magnitude**

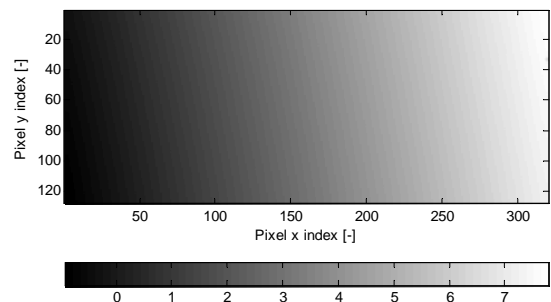
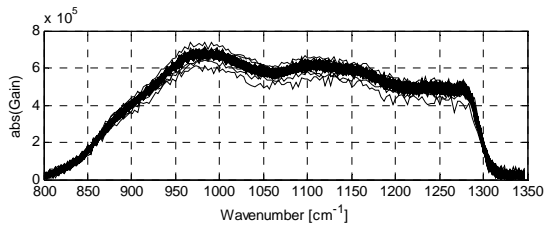


**Figure 8: Spatial map of the gain phase shift in metrology fringes**

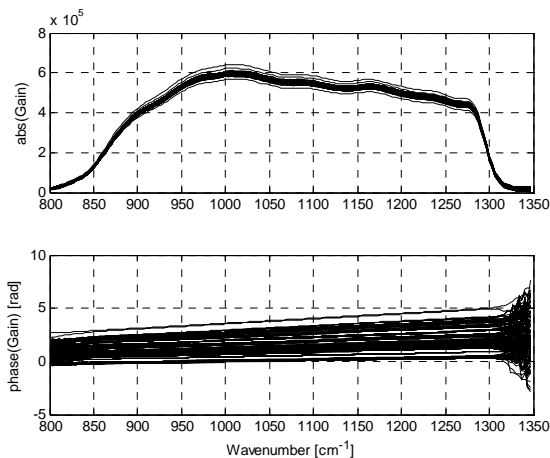
Figure 9 shows the magnitude of the gain of one typical pixel, for all the 161 radiometric calibrations of the two field campaigns. This result shows that the spectral shape of the gain magnitude has not changed significantly

during the entire time lapse. This is in line with our hypothesis that the pixel dependant shape is due to detector channelling. The temperature of the FPA is well controlled, and thus, the channeling effect is constant. Given this observation, the analysis of the gain magnitude will simply consider the fluctuations that are observed on the spectral average of the gain magnitude, between 900 and 1250  $\text{cm}^{-1}$ . Also, the results for all the good pixels are averaged together in order to reduce the noise level. "Bad" pixels - roughly 3% of the detector pixels - are excluded from this averaging.

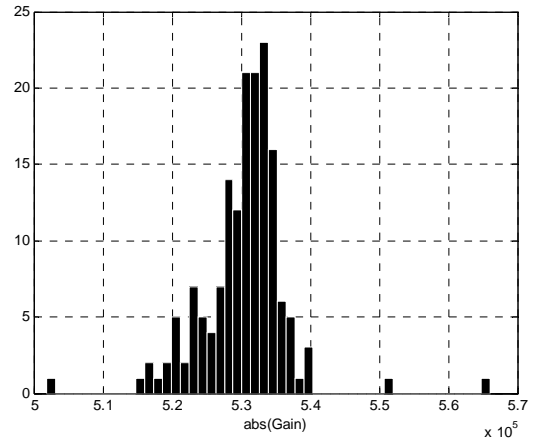
Figure 10 shows the magnitude and phase of the gain, averaged for all good pixels, for all the radiometric calibrations of the two field campaigns. Figure 11 shows the distribution of the gain magnitude, averaged between 900 and 1250  $\text{cm}^{-1}$ .



**Figure 9: Magnitude of the gain of one typical pixel for all the radiometric calibrations**

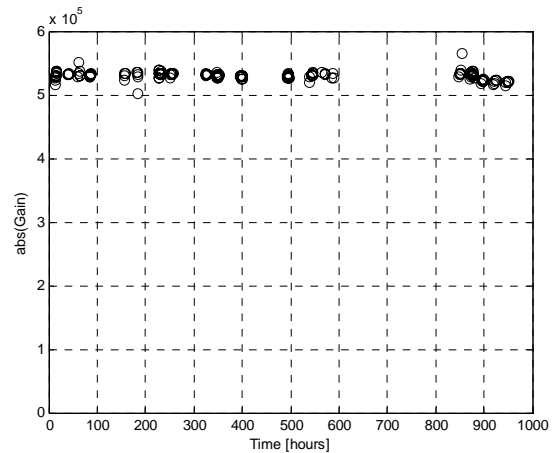


**Figure 10: Measurements of the magnitude and phase of the gain, averaged for all pixels**

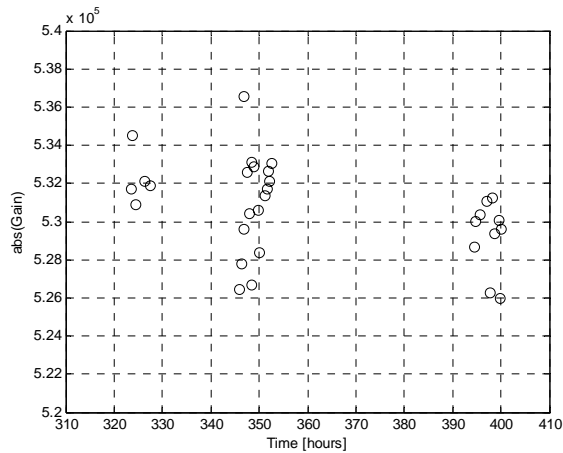


**Figure 11: Distribution of the average gain magnitude over the field campaigns duration**

One important aspect of the radiometric stability is dictated by the amplitude fluctuations of the gain. Such fluctuations can be mainly caused by variations of the detector responsivity, interferometer modulation efficiency or optics transmittance. In this case, the overall fluctuation of the amplitude of the gain magnitude shows a standard deviation of 1.6% over the entire time lapse, which is relatively small. A 1.6% error on the gain magnitude estimation leads to a direct radiance error of 1.6%. Further analysis has shown that these gain magnitude fluctuations are not directly correlated to the sensor temperature. Figure 12 shows the gain magnitude as a function of time (the zero time reference is 7 June 2005 at midnight). Figure 13 presents a zoomed view on the average gain magnitude over a four-day period.

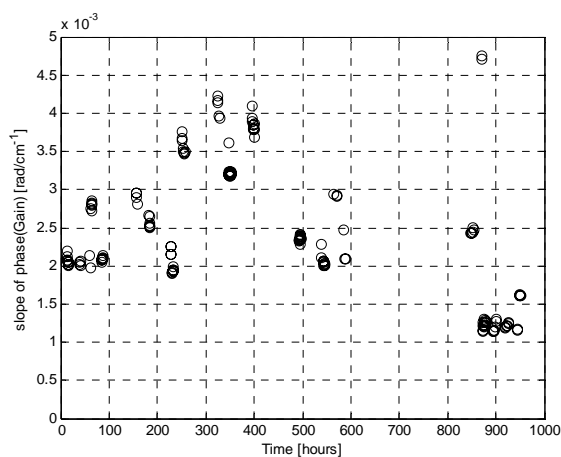


**Figure 12: Average magnitude of the gain over time**



**Figure 13: Average magnitude of the gain over time zoomed over a four-day period**

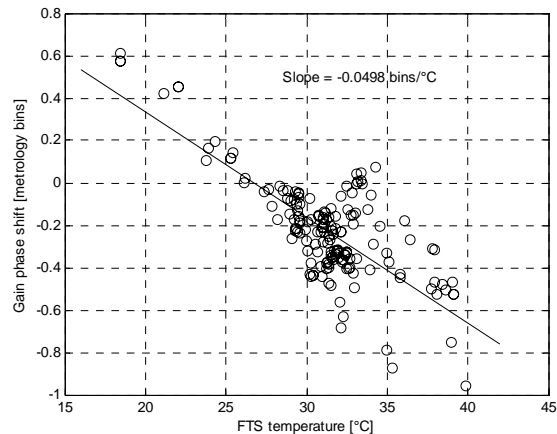
Another crucial aspect of the radiometric stability is dictated by the gain phase fluctuations. A variation in the gain phase slope is directly related to a shift of OPD in the interferogram. At each start-up, the FIRST sensor initializes its metrology counter based on a mechanical limit switch. This mechanism is known to be repeatable within a few metrology fringe counts (a few micrometers). Therefore, it is expected that for all the sensor start-ups, the interferogram sampling should be randomly shifted by a few points. This explains the rich number of slopes that can be seen in the phase of the gain of Figure 10. Figure 14 shows the slope of the phase of the gain as a function of time. It is clear that the slope varies much less significantly during a day than between days, after a sensor shut down and start-up.



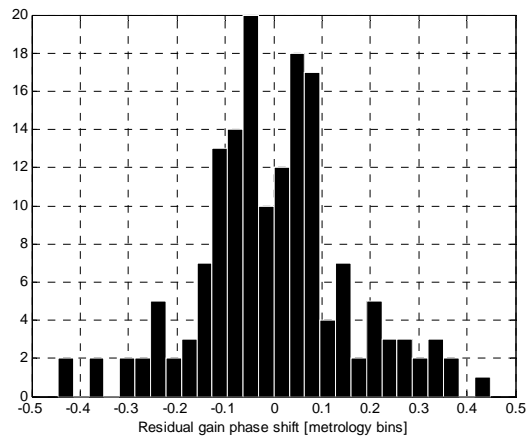
**Figure 14: Average slope of the gain phase over time**

The large phase slope steps can be corrected, knowing that they are caused by an interferogram sampling shift of an integer number of points. Once this major correction is executed, it is interesting to look at the relation between the slope of the gain phase and the sensor temperature, as shown in Figure 15. The slope of the phase is converted in units of metrology fringe shifts.

A reasonable linear correlation can be seen in Figure 15. Figure 16 shows the distribution of the gain phase shift after the linear correction is applied.

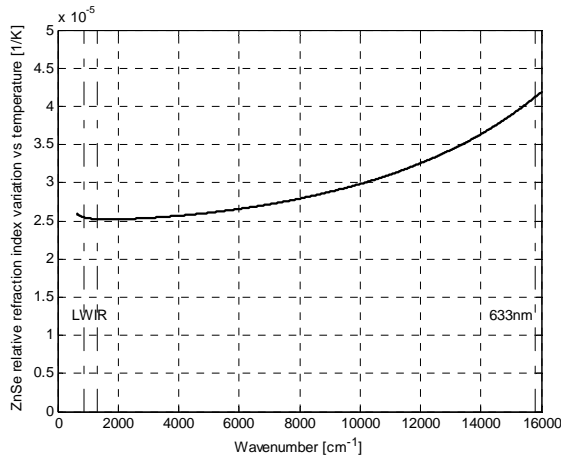


**Figure 15: Gain phase shift as a function of the sensor temperature after alignment of the interferograms**



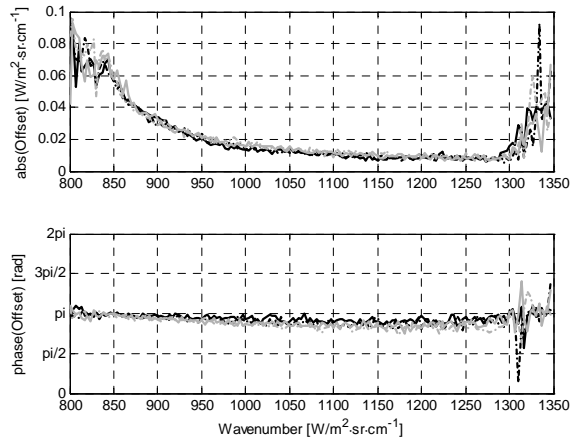
**Figure 16: Distribution of the gain phase shift in the spectra after alignment of the interferograms and after linear correction for the sensor temperature**

The linear correlation of Figure 15 can be attributed to the chromatic dispersion of the beamsplitter. It is known that a change of temperature of the interferometer beamsplitter (made from ZnSe) changes its refractive index, thus leading to a chromatic dispersion phenomenon. This generates an OPD (optical path difference) variation that depends on the wavelength. The effect of this is that the instrument phase changes by a different factor for the metrology (at 633 nm) than for the scene signal (between 7.8 and 11.7  $\mu\text{m}$ ). This phenomenon is minimized by using a compensated beamsplitter, but since compensation is never perfect in practice, this effect remains present. Figure 17 shows the ZnSe refractive index temperature coefficient at 300 K. It shows that the refractive index varies almost twice as much at 633 nm than in the spectral range of the sensor. Data on the ZnSe refractive index are taken from [7].



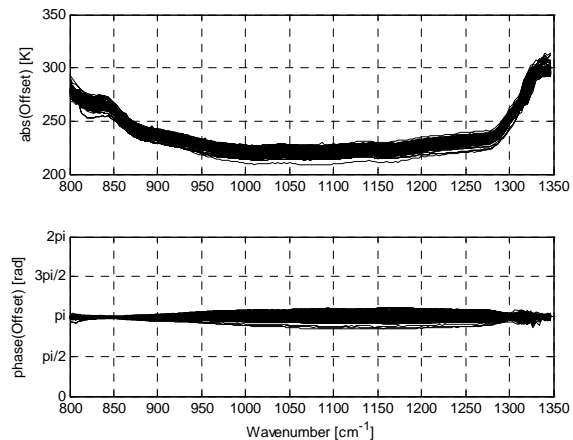
**Figure 17: ZnSe refractive index variation with temperature around 300 K as a function of wavenumber**

Figure 18 shows the magnitude and phase of the radiometric offset of 4 random pixels of the sensor. The offset of all pixels is very similar to the radiance spectrum of a cold blackbody. This is because the sensor has a good transmittance, and thus a low radiometric offset. Furthermore, since the instrument is in a 2-port configuration, the contribution of the output port to the radiometric offset is very low, as the detector is cooled down to 68 K.



**Figure 18: Magnitude and phase of the offset of 4 random pixels**

Figure 19 shows the magnitude of the offset of all the calibration measurements, averaged for all the good pixels, in units of brightness temperature. The phase of the offset is also shown. In addition, the spatial map of the offset magnitude is shown in Figure 20.



**Figure 19: Magnitude of the offset in brightness temperature, averaged for all pixels**

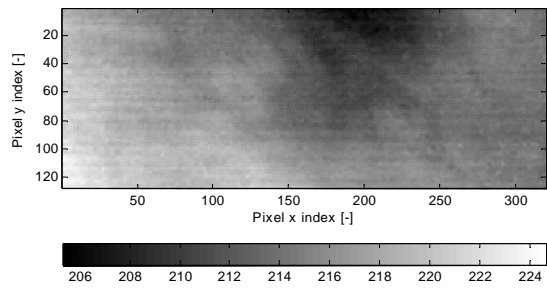


**Figure 20: Spatial map of the offset magnitude in brightness temperature [K]**

The offset is very low (~215 K), which indicates that the shot noise coming from the instrument radiance is minimized. This helps to reduce the noise level, since the FIRST is shot noise limited. The offset magnitude is also strongly related to the sensor temperature, as shown in Figure 21. A change of the sensor temperature always has a direct impact on the radiometric offset, and this impact can be well corrected with a simple linear correction, since the sensor temperature is known at all times.

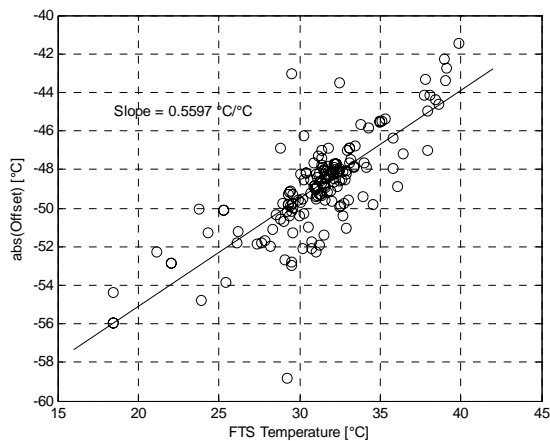


**Figure 21: Offset magnitude in brightness temperature as a function of the sensor temperature**

Figure 22 shows the distribution of the offset after the correction. Once this correction is applied, the standard

deviation of the offset amplitude becomes equal to 4.6% in radiance, or a 1 K radiance error. An error of this magnitude on the radiometric offset generates a 0.6% error on the radiance accuracy of the sensor. Note that the 0.56 slope of the offset temperature relative to the sensor temperature indicates that approximately 56% of the offset seen by the detector comes from sensor self-radiance, while the remaining 44% of the offset comes from the inside of the dewar, which is constant at 68 K.

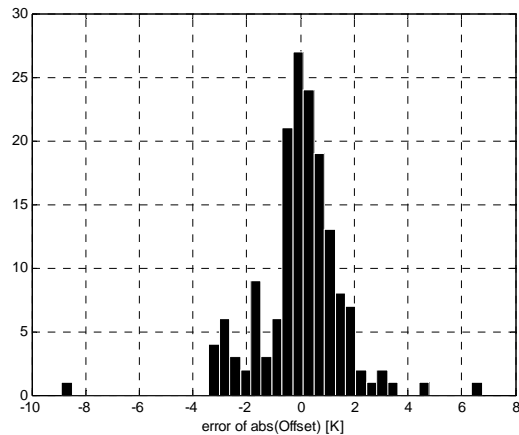


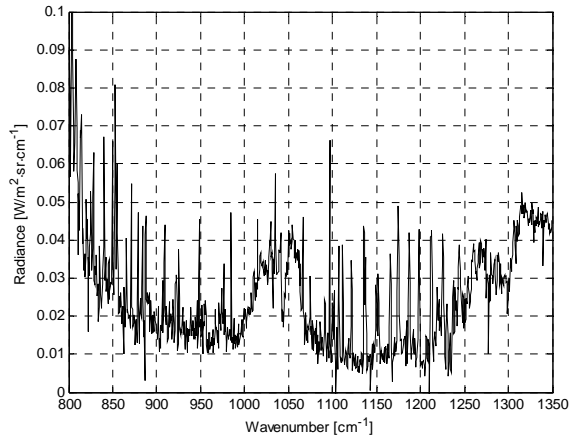
**Figure 22: Distribution of the offset magnitude in brightness temperature after a linear correction for the sensor temperature**

The phase of the offset is centered on  $\pi$  (see Figure 19), which is expected for radiance that comes from the output port. The fluctuations around  $\pi$  exhibit a shape indicating the presence of dispersion, but of unknown origin.

Assuming that the errors are not correlated, the overall radiance accuracy can be estimated by calculating the RSS (root sum square) of all the error contributions that were identified in this section. The result indicates a total radiance accuracy of 1.8% ( $\sqrt{1.6\%^2 + 0.6\%^2 + 0.6\%^2}$ ). We emphasize that this level of accuracy is obtained with simple temperature compensation and without recalibrating the instrument by measuring calibration blackbodies. It is also implied that a phase correction is performed when the sensor is turned off and back on.

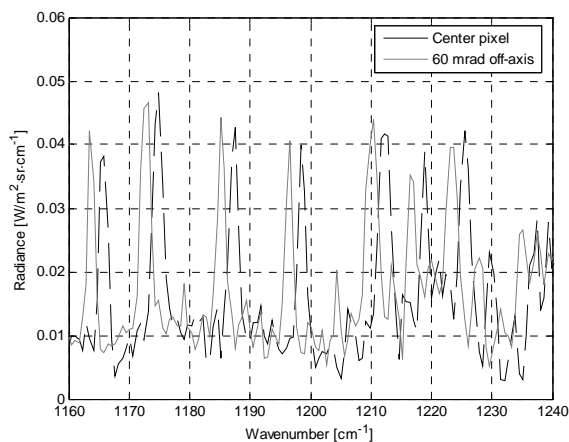
## 6. Spectral Calibration

The sensor spectral calibration was done by performing clear sky measurements with the sensor, at a high spectral resolution ( $0.5 \text{ cm}^{-1}$ ). The measurement was made at this resolution for a  $320 \times 128$  pixels window. Figure 23 shows the radiance spectrum measured for one pixel. Water vapor emission lines are seen in the  $1150$  to  $1250 \text{ cm}^{-1}$  region. Also, ozone emission is seen in the  $1000$  to  $1075 \text{ cm}^{-1}$  region.



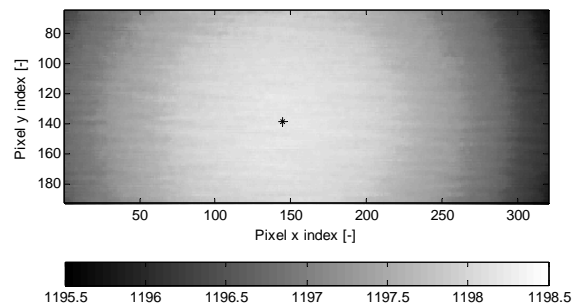
**Figure 23: Sky radiance measurement for a single pixel**

Figure 24 shows the radiance of 2 pixels around the water vapor lines. The first pixel is on the optical axis, while the other pixel is on the right edge ( $60 \text{ mrad}$  off-axis). One can notice a spectral shift of approximately  $2 \text{ cm}^{-1}$  between the two spectra. This is caused by the ILS (instrument lineshape).



**Figure 24: Sky radiance measurement for 2 pixels, zoomed on water vapor emission lines**

It is possible to correct for this effect by simply multiplying the wavenumber axis of each pixel by the cosine of its off-axis angle. More sophisticated ILS correction models can also be used, but this simple correction yields excellent results for spectral calibration. This is especially true because of the small IFOV of the sensor. Figure 25 shows the  $1198.18 \text{ cm}^{-1}$  water vapor line position as a function of the position in the FPA. Spatial median filtering is used to eliminate the bad pixels. The position varies between  $1195.67$  and  $1198.18 \text{ cm}^{-1}$ . However, after applying the simple correction mentioned above, the standard deviation of the line position becomes equal to  $0.3 \text{ cm}^{-1}$ , inferior to the spectral resolution used of  $0.5 \text{ cm}^{-1}$ .



**Figure 25: Spatial map of the measured water vapor emission line position in wavenumber  $[\text{cm}^{-1}]$**

The optical axis is determined by identifying the pixel that has the highest emission line position prior to the correction. The pixel coordinates are  $x = 145$  and  $y = 138$  (identified by an asterisk in Figure 25). Once this is done, the “effective” metrology wavelength is determined, such that the experimental results matches the theoretical line position. This effective metrology wavelength can then be used to generate the calibrated spectral axis for the subsequent measurements. This characterization of the effective wavelength can be performed once, and is expected to remain valid for the sensor lifetime with an excellent accuracy. Analyses will be conducted in order to quantify the stability of the spectral calibration over time.

## 7. Conclusion

It was shown in this paper that over a period of 40 days, the radiance accuracy of the FIRST sensor remains better than 2%, with a single radiometric calibration. This assumes that the sensor temperature is stabilized, or that a linear correction based on the instrument temperature is applied on the gain phase and offset magnitude. This also implies that a phase correction is performed when the sensor is turned off and back on. This radiometric stability measured in the field underlines the quality of the FIRST sensor.

It was also shown in this paper that a simple spectral calibration of the FIRST sensor ensures a spectral accuracy of  $0.3 \text{ cm}^{-1}$  for each pixel, when using a  $0.5 \text{ cm}^{-1}$  spectral resolution. This assumes that a simple correction for the instrument lineshape is performed. The stability of the spectral calibration over time will be characterized in future tests.

## Acknowledgements

Telops would like to gratefully acknowledge the data contribution of the Johns Hopkins University Applied Physics Laboratory. Telops would also like to thank Dstl for the invitation to a field-campaign in June 2005, as well as the Department of National Defence of Canada for funding the production of the FIRST sensor and our participation to the field-campaign under a Defence Industrial Research (DIR) program.

## REFERENCES

- [1] H.E. Revercomb, H. Buijs, H.B. Howell, D.D. Laporte, W.L. Smith, and L.A. Sromovsky, *Radiometric calibration of IR Fourier transform spectrometers: Solution to a problem with the high-resolution interferometer sounder*; Applied Optics, vol. 27, issue 15, pp. 3210-3218, August 1988.
- [2] A. Villemaire, M. Chamberland, J. Giroux, R. L. Lachance, J.-M. Thériault, *Radiometric calibration of FT-IR remote sensing instrument*; Proc. SPIE Vol. 3082, pp. 83-91, Electro-Optical Technology for Remote Chemical Detection and Identification II; Mahmoud Fallahi, Ellen A. Howden; Eds., July 1997.
- [3] M. Chamberland et al., *Advancements in field-portable imaging radiometric spectrometer technology for chemical detection*, Proc. SPIE Vol. 5416, pp. 63-72, Chemical and Biological Sensing V; Patrick J. Gardner; Ed., August 2004.
- [4] V. Farley et al., *Development and testing of a hyper-spectral imaging instrument for field spectroscopy*, Proc. SPIE Vol. 5546, pp. 29-36, Imaging Spectrometry X; Sylvia S. Shen, Paul E. Lewis; Eds., October 2004.
- [5] M. Chamberland et al., *Development and testing of a hyper-spectral imaging instrument for standoff chemical detection*, Proc. SPIE Vol. 5584, pp. 135-143, Chemical and Biological Standoff Detection II; James O. Jensen, Jean-Marc Theriault; Eds., December 2004.
- [6] A. Vallières et al., *High-Performance Field-Portable Imaging Radiometric Spectrometer Technology For Chemical Agent Detection*, Proc. SPIE Vol. 5590, pp. 211-219, Optically Based Materials and Optically Based Biological and Chemical Sensing for Defence II; John C. Carrano, Arturas Zukauskas, Anthony W. Vere, James G. Grote, François Kajzar; Eds., October 2005.
- [7] C. A. Klein, R. P. Miller, and D. L. Stierwalt, *Surface and bulk absorption characteristics of chemically vapor-deposited zinc selenide in the infrared*, Applied Optics, vol. 33, issue 19, pp. 4304-4313, 1994.